Available online at www.sciencedirect.com
ScienceDirect
Acta Materialia 82 (2015) 414–423
Acta MATERIALIA
www.elsevier.com/locate/actamat

On the room temperature deformation mechanisms of a Mg–Y–Zn alloy with long-period-stacking-ordered structures

Jin-Kyung Kim, Stefanie Sandlöbes* and Dierk Raabe*

Max-Planck-Institut für Eisenforschung GmbH, Max-Planck-Straße 1, 40237 Düsseldorf, Germany

Received 14 August 2014; revised 18 September 2014; accepted 18 September 2014

Abstract—We present a transmission electron microscopy study on the room temperature deformation mechanisms in a $Mg_{97}Y_2Zn_1$ (at.%) alloy with long-period-stacking-order (LPSO) phase. The alloy consists of α-Mg matrix with platelet-shaped LPSO precipitates 3–5 nm thick and interdendritic LPSO (18R structures) phase grains. The interdendritic LPSO phase was found to deform either by kink-banding in conjunction with basal <a> slip or by basal <a> slip and the formation of dislocation walls. No orientation dependence of these different deformation modes was observed. The α-Mg matrix deforms by basal <a> slip and pyramidal <c + a> slip. No twinning was observed in the α-Mg matrix during room temperature deformation. The elastic modulus mismatch between α-Mg matrix and LPSO plates is suggested to be the main source for activating non-basal dislocations. The combination of the soft α-Mg matrix strengthened by LPSO precipitates and harder "bulk" interdendritic LPSO grains is suggested to contribute to the well-known good mechanical properties of Mg-LPSO alloys at room temperature.

Keywords: Magnesium alloy; Long-period-stacking-ordered structure; Dislocations; Deformation structures; Transmission electron microscopy

1. Introduction

Magnesium (Mg)-based alloys are attractive for many engineering structural applications owing to their low density, high specific strength, good castability and recyclability [1]. However, the low strength and poor room temperature formability of Mg alloys have hindered their wider application. During the past decade, Mg–Y–Zn alloys containing long-period-stacking-ordered (LPSO) structures have received considerable attention owing to their excellent mechanical properties [2–7].

The LPSO phases have the same (0001) basal plane as Mg while their stacking periodicity is lengthened 18- or 14-fold, respectively, along the c-axis relative to the c-axis length of pure Mg [8–16]. LPSO structures consist of Y- and Zn-enriched building blocks which have an ABCA stacking sequence of closely packed planes [9,12,13,15]. Each of these building blocks has a shear component with respect to the α-Mg matrix phase since Shockley partial dislocations exist at the ends of these blocks [12,17]. The 18R phase is formed during solidification of Mg–Y–Zn alloys [3], and is gradually transformed to 14H after appropriate heat treatments in the temperature range of 350–500 °C [10,15].

The LPSO structures have been regarded as a strengthening phase [6,16,25,26]. However, the active deformation mechanisms that result in increased strength and ductility with respect to pure Mg are not well understood and—in part—remain controversial [3,6,7,16,18–27].

Chino et al. [26] reported a hardness improvement caused by the LPSO structure from indentation experiments. Matsuda et al. [20,27] studied the interaction between twinning and dislocations with the LPSO structure in a rapidly solidified Mg–Zn–Y alloy. They showed that the growth of deformation twins in the α-Mg matrix was prevented by densely populated LPSO precipitates, thereby providing strengthening [18]. Their transmission electron microscopy (TEM) study revealed no trace of basal plane <a> dislocation in LPSO structures, which is believed to be due to an increase in the critical resolved shear stress (CRSS) for basal dislocation slip. On the other hand, occurrence of <c + a> dislocations indicated the activation of non-basal slip systems, thus improving the ductility of the LPSO structure containing alloy. However, Hagihara et al. [18] insisted that basal slip was the dominant deformation mode in the LPSO phase during the compression of directionally solidified $Mg_{88}Zn_5Y_7$ (at.%) crystals. Additionally, the formation of kink bands has been frequently observed during the deformation of LPSO phases [18,22,28]. Shao et al. [22] examined the deformation mechanisms of $Mg_{97}Y_2Zn_1$ (at.%) alloy during compression at 300 °C. They confirmed that the formation of kink bands of the LPSO phase was closely related to the generation and synchronized slip of dislocation pairs of opposite sign on basal planes during hot compression.

However, no detailed studies on the room temperature deformation mechanisms of bulk Mg-LPSO alloys are available. The aim of our study is to contribute to a better

---

* Corresponding authors; e-mail addresses: s.sandloebes@mpie.de; d.raabe@mpie.de

http://dx.doi.org/10.1016/j.actamat.2014.09.036

understanding of the room temperature deformation mechanisms of Mg-LPSO alloys. Understanding the complex deformation mechanisms of bulk Mg-LPSO alloys is essential for the design and application of room temperature formable Mg–Y–Zn sheet materials. Therefore, the present study examines the room temperature deformation mechanisms of a cold-rolled $Mg_{97}Y_2Zn_1$ alloy, in both the α-Mg matrix and in the LPSO phase, using TEM.

2. Experimental methods

A $Mg_{97}Y_2Zn_1$ (at.%) alloy was prepared using induction melting under a 15 bar pressure Ar atmosphere. The cast material was solution-treated at 500 °C for 2.5 h followed by water quenching. Some parts of the solution-treated material were cold rolled to 5% total thickness reduction in order to observe the deformation microstructures and active deformation mechanisms.

The samples for scanning electron microscopy (SEM) were prepared by sectioning the plane of the normal direction (ND) and the rolling direction (RD). Mechanical grinding was followed by 1 μm diamond polishing. The samples were then electropolished using the commercial electrolyte AC2 Soft cooled to −10 °C. SEM observation was conducted on a JEOL JSM6500 microscope equipped with a field emission gun and an energy-dispersive X-ray spectrometry (EDS) detector.

The samples for TEM were cut into discs 3 mm in diameter and 1 mm height from the ND–RD plane. The discs were ground to a thickness of 150–200 μm, then twin-jet electropolished in a solution of 5.3 g lithium chloride, 11.2 g magnesium perchlorate, 500 ml methanol and 100 ml 2-butoxy-ethanol at −30 °C. The bright-field (BF), weak-beam dark-field (WBDF) TEM images and related selected-area diffraction patterns (SADPs) were obtained with a Philips CM20 instrument operating at 200 kV. All the WBDF images were taken with g-2g diffraction conditions. High-angle annular dark-field scanning transmission electron microscopy (HAADF-STEM) images were obtained with a JEOL JEM-2200FS instrument operating at 200 kV. Most of the TEM observations were conducted such that the incident beam direction was nearly parallel to either $[1\bar{2}10]_\alpha$ or $[1\bar{1}00]_\alpha$. In this condition, the basal planes were inclined nearly parallel to the incident electron beam direction so that the trace of the basal planes could be easily determined from the TEM images. Due to tilting limit of the TEM and sample orientation, complete Burgers vector analysis was not possible. However, the type of the dislocations, i.e. <a>, <c> and <c + a> dislocations, could be determined using the $g \cdot b = 0$ invisibility criterion under several different two-beam conditions.

3. Results

3.1. Solution-treated microstructure of $Mg_{97}Y_2Zn_1$ alloy

Fig. 1a shows the SEM image of the solution-treated and quenched material. The microstructure consists of the α-Mg matrix with dark contrast and the interdendritic LPSO phase with grey contrast. The interdendritic LPSO phase has a size of 10–50 μm, and its volume fraction is determined to be 27 vol.% using automated SEM image analysis of a series of secondary electron (SE) micrographs. The typical α-Mg matrix grain size is ∼100 μm, and the crystal orientations are nearly random without a strong basal texture component. The average chemical compositions of the α-Mg matrix and the interdendritic LPSO phase are determined to be Mg–0.56Y–0.26Zn (at.%) and Mg–5.12Y–3.92Zn (at.%), respectively, using SEM-EDS.

The α-Mg matrix is characterized in more detail by the TEM BF image shown in Fig. 1b. A high density of thin plate-type defects is found to be aligned along the basal plane trace indicated by the white dashed line. No streaks between the primary and (0002) basal diffraction beam are found in the SADP of the region. Fig. 1c shows an HAADF-STEM micrograph of the α-Mg matrix. The plates along the basal plane have a brighter contrast than the α-Mg matrix, revealing that they are enriched with Y and Zn. This allows the identification of the thin platelets inside the α-Mg matrix grains as LPSO precipitates.

Fig. 2 shows a HAADF-STEM micrograph of the interdendritic LPSO phase. A high density of dark plates is observed while most regions of the phase show bright contrast. The plates with dark contrast are assumed to be bands of α-Mg layers depleted in Y and Zn. Such α-Mg layers inside LPSO grains were observed before in a solution-treated Mg–8Y–2Zn–0.6Zr (wt.%) alloy [15]. The LPSO phase is determined to have 18R structure from the SADP shown in Fig. 2c. The $[1\bar{2}10]_\alpha$ pattern clearly shows extra diffraction spots at the $\pm 1/3(0001)_\alpha$ and the $\pm 2/3(0001)_\alpha$ positions.

3.2. Cold-rolling microstructure of $Mg_{97}Y_2Zn_1$ alloy

The microstructure after 5% cold rolling is characterized using SEM and TEM. Fig. 3 shows back-scattered electron (BSE)-SEM micrographs of the 5% cold-rolled material. The Vickers microhardness is increased from 70 ± 5 to $80 \pm 13\ HV_{0.5}$ after cold rolling. In some regions of the material kink bands are formed in the interdendritic LPSO phase as seen in Fig. 3a, while in other regions of the same sample the formation of kink bands is not observed (see Fig. 3b). No orientation dependence of kink banding was observed in this study. The characteristics of the observed kink bands can be seen in detail in Fig. 3c and d. The kinking angle ranges from 30° to 60°. In the vicinity of the kink bands of the interdendritic LPSO phase, thin LPSO plates in the α-Mg matrix are also found to be kinked as shown in Fig. 3c.

Due to the observed inhomogeneous deformation microstructures, TEM observations were systematically conducted in the various regions and revealed different deformation characteristics. The deformation features of the interdendritic LPSO phase can be seen in Figs. 4 and 5. Fig. 4a is a HAADF-STEM micrograph of the deformed interdendritic 18R phase which clearly shows the existence of kink bands. The $[1\bar{2}10]_\alpha$ diffraction patterns from area A to D are also presented. The kink boundaries are indicated by dashed lines. From area A to B, the basal plane is rotated clockwise with a rotation angle of ∼15°. On the other hand, the lower kink boundary from area B to C is rotated counterclockwise with a rotation angle of ∼25°. However, separate dislocation contrast is not resolvable in the kink boundaries probably due to the high misorientation angle. The TEM BF micrographs taken with two-beam conditions of $g = \{00,18\}$ (i.e. $\{00018\}$), and $g = \{1\bar{1},1\}$ from area B of Fig. 4a are presented in

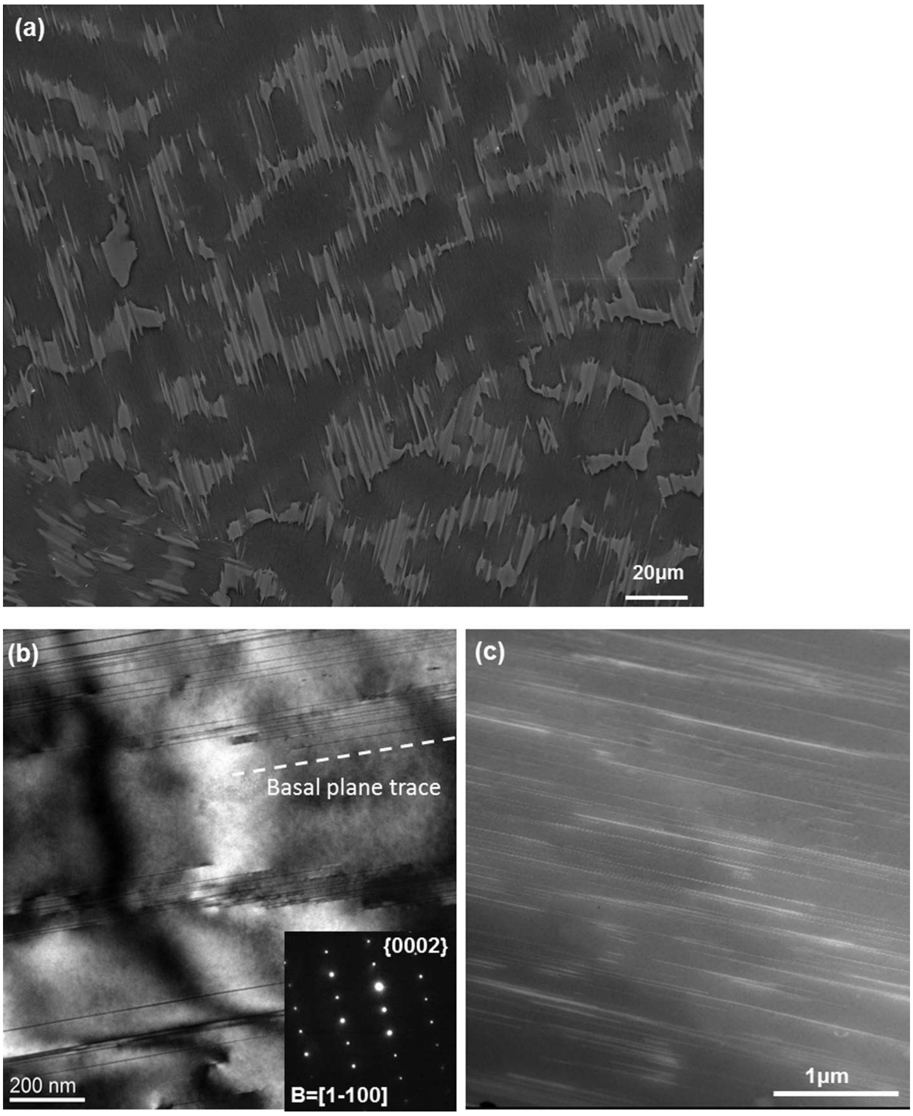

Fig. 1. (a) SEM image showing the α-Mg grains (dark contrast) and interdendritic LPSO (grey contrast) in the solution-treated material; (b) TEM bright-field (BF) image and selected-area diffraction pattern (SADP) and (c) high-angle annular dark-field scanning transmission electron microscopy (HAADF-STEM) micrograph of the solution-treated $Mg_{97}Y_2Zn_1$ alloy for 2.5 h at 500 °C showing thin LPSO precipitates inside the α-Mg matrix. The basal plane trace is indicated by the white dashed line.

Fig. 4b to characterize the types of dislocations. In the two-beam condition of $g = \{00,18\}$, only dislocations with a <c> component should be visible. However, the fact that no dislocation contrast appears in this diffraction condition, except the contrast of the α-Mg plates, indicates that dislocations with a <c> component do not exist in this region. In the two-beam condition of $g = \{\bar{1}1,1\}$, dislocations parallel to the basal plane are observed. Therefore, basal <a> dislocations seem to occur concomitant with kink banding in the interdendritic LPSO phase which forms kink bands. This is probably due to the fact that the formation of kink bands in the LPSO phase is closely related to the generation and synchronized slip of dislocation pairs of opposite sign on basal planes during deformation [22].

The interdendritic LPSO phase which had not formed kink bands after 5% cold rolling was investigated separately. Fig. 5a shows TEM two-beam BF micrographs of such a region in the microstructure. Three main features are observed: long plates, short line-type defect features between the long plates, and individual extended dislocation walls. Kink bands are not observed in this area. The long plates are assumed to be Y- and Zn-depleted α-Mg bands as observed in the solution-treated microstructure (Fig. 2). The formation of an elongated dislocation wall is observed between the upper and lower areas of the grain (Fig. 5a). A slight rotation of the basal plane by ~1° between the upper and lower portions of the grain was determined by a comparison of the corresponding $[1\bar{2}10]_\alpha$ diffraction patterns on either side of the dislocation wall (regions A and B in Fig. 5a). In the two-beam condition $g = \{00,18\}$ only the short line-type defects which are parallel to the basal plane are in contrast as indicated by white arrows (Fig. 5b). Those defects are not dislocations, but possibly short Mg plates with depleted Y and Zn atoms. Fig. 5c shows a WBDF micrograph of the same region with $g = \{1\bar{1},10\}$. The short Mg plates which appear contrasting in Fig. 5b show the contrast of narrow stacking fault fringes under WBDF conditions. This again suggests that

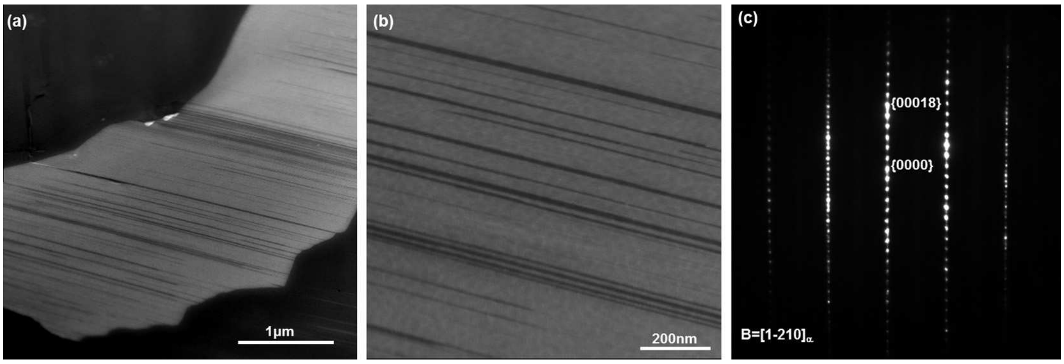

Fig. 2. (a) HAADF-STEM image of the solution-treated $Mg_{97}Y_2Zn_1$ alloy for 2.5 h at 500 °C showing the interdendritic LPSO phase. The regions with dark contrast are Y- and Zn-depleted α-Mg layers. (b) Enlarged image of (a), (c) SADP obtained from interdendritic LPSO which represents reflections of 18R structure. The electron beam is parallel to $[1\bar{2}10]_{\alpha}$.

these are non-ordered thin α-Mg plates which appear as stacking faults from the viewpoint of the LPSO phase. Another kind of short line-type defects which are indicated by arrows is parallel or slightly inclined with the trace of the basal plane. These defects are identified as basal <a> dislocations. Therefore, basal <a> slip and the formation of dislocation walls are found as main deformation modes in those interdendritic LPSO grains that have not formed kink bands.

The deformation features of the α-Mg matrix are shown in Figs. 6–9. TEM BF images of the α-Mg matrix with kinked LPSO plates are shown in Fig. 6. Under diffraction conditions with $g = \{0002\}$, dislocations with a <c> component are clearly visible. From the invisibility criterion analysis, the dislocations are determined to be <c + a> dislocations with the Burgers vector of $b = a/3[\bar{2}113]$ on the first-order pyramidal plane (10–11). From the observed contrast of <c + a> dislocations, it seems possible that cross-slip of <c + a> dislocations occurs along LPSO building blocks.

The α-Mg matrix without kinked LPSO plates was also investigated. Fig. 7 shows TEM BF and WBDF images taken under four different two-beam conditions ($g = \{10\bar{1}0\}, g = \{10\bar{1}1\}, g=\{0002\}, g = \{\bar{1}011\}$). LPSO plates with stacking fault-like fringes and dislocations are observed. It should be noted that all dislocations are out

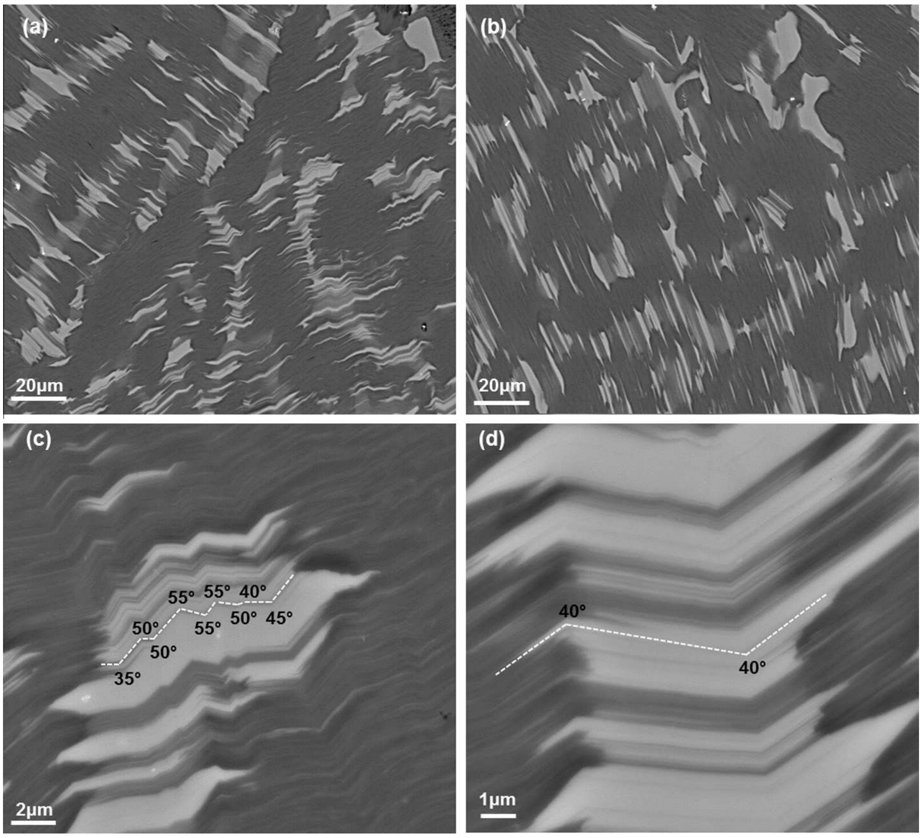

Fig. 3. Backscattered electron (BSE)-SEM image of 5% cold-rolled $Mg_{97}Y_2Zn_1$ (engineering strain) showing regions (a) with kink bands and (b) without kink bands. (c, d) Enlarged images showing the kink angle and kink width of the observed kink bands.

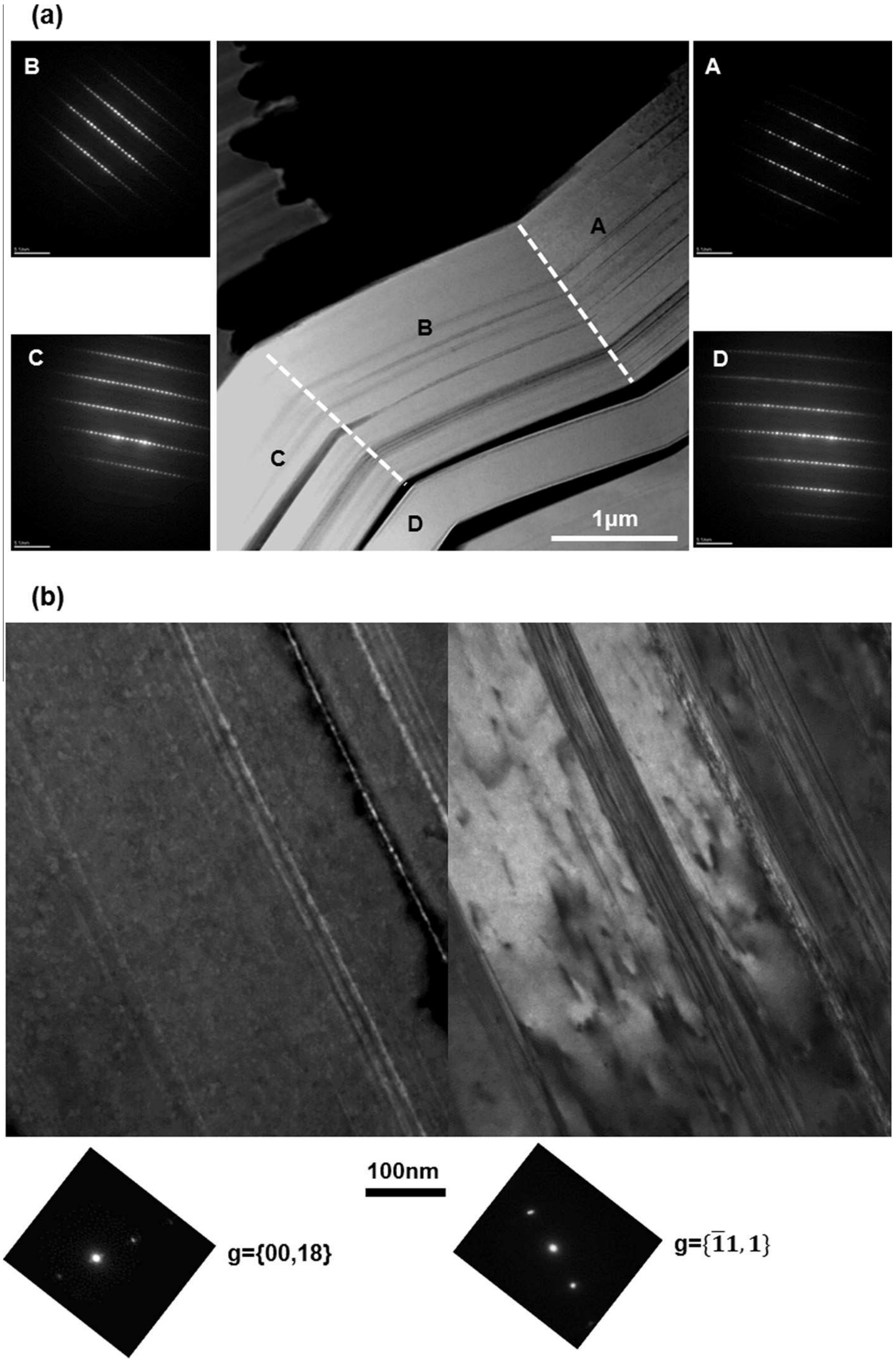

Fig. 4. (a) HAADF-STEM image of 5% cold-rolled $Mg_{97}Y_2Zn_1$ showing interdendritic LPSO deforming by kink banding. The $[1\bar{2}10]_\alpha$ SADPs from area A to D are presented. The kink boundaries are indicated by dashed lines. (b) TEM BF images of area B in (a) with two-beam condition of g = {00,18}(left), and g={$\bar{1}$1, 1} (right).

of contrast in the two-beam condition of g = {0002}. This suggests that these dislocations do not have a <c> component. Analysis of the four different two-beam conditions presented reveals that the dislocations are either perfect basal <a> or partial basal <a> dislocations. The absence of stacking fault fringes in the dislocation contrast and the fact that no dislocation dissociation was observed indicates that the dislocations are highly possibly perfect basal <a> dislocations. Fig. 8 shows the TEM WBDF image of the α-Mg matrix in a different region. The trace of the basal plane is indicated by the white dashed line. Most dislocations are parallel with the trace of the basal plane. This suggests that they are basal <a> dislocations. On the other hand, some dislocation segments out of the trace of the basal plane are indicated by white arrows. Those dislocations do not have a <c> component since dislocations with a <c> component should be invisible under a diffraction condition of g = {$11\bar{2}0$}. It is known that <a> -type dislocations with segments out of the basal planes are most certainly non-basal (prismatic or pyramidal) <a> dislocations

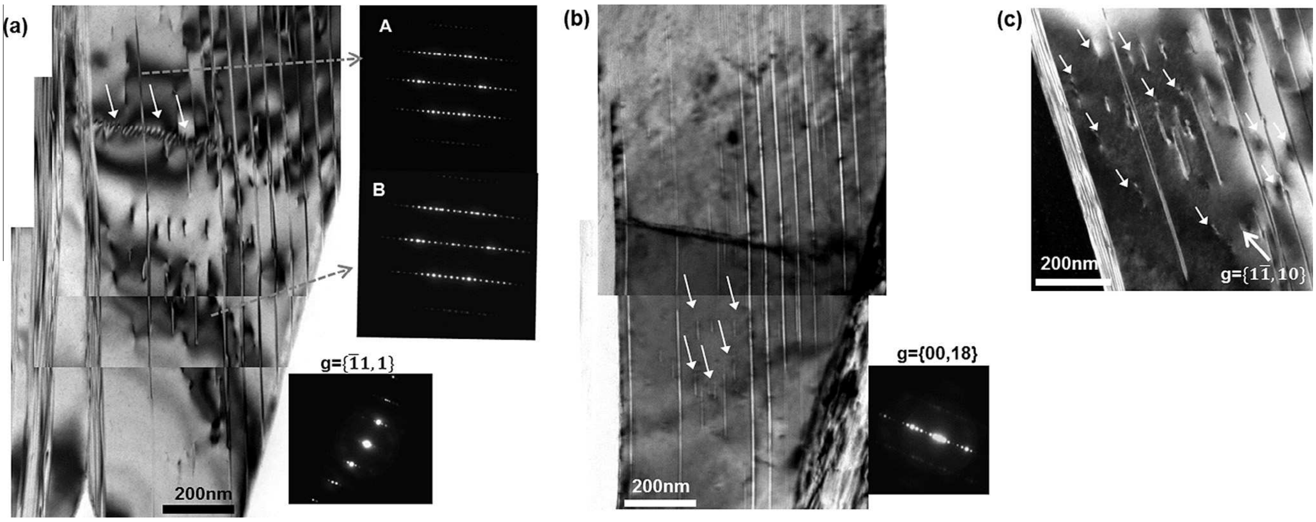

Fig. 5. TEM BF images of 5% cold-rolled $Mg_{97}Y_2Zn_1$ showing interdendritic LPSO without kink bands with two-beam condition of (a) g = {$\bar{1}$1, 1 } and (b) g = {00,18}. The $[1\bar{2}10]_\alpha$ SADPs from area A and B are also presented in (a). A dislocation wall is indicated by an arrow in (a), short Mg plates are indicated by white arrows in (b). (c) WBDF image of the same area showing basal <a> dislocations indicated by white arrows.

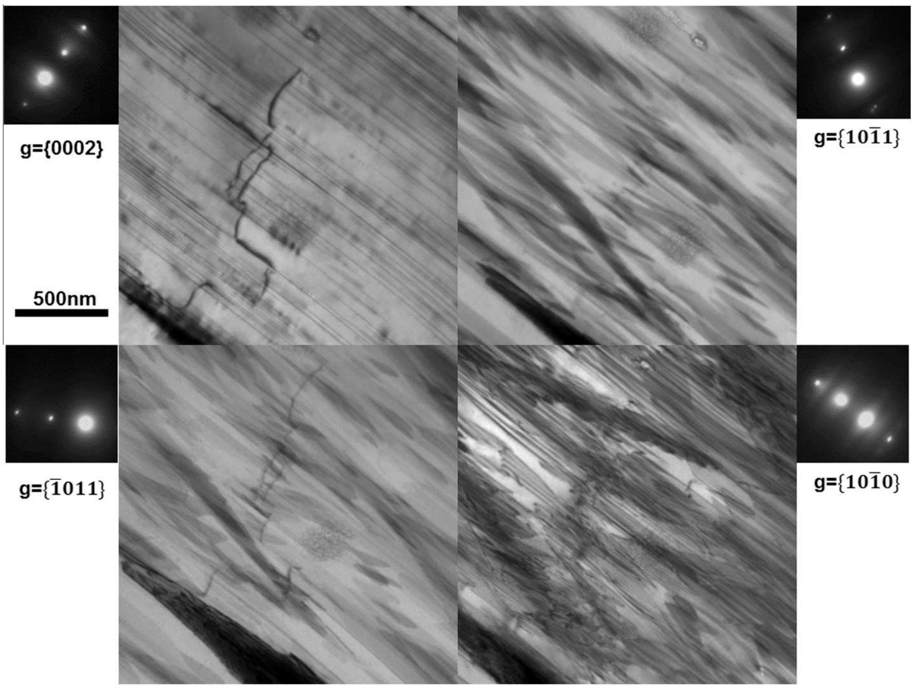

Fig. 6. TEM BF images of 5% cold-rolled $Mg_{97}Y_2Zn_1$ alloy showing α-Mg matrix with kinked LPSO precipitates under four different two-beam conditions. The contrasting dislocations are determined to be <c + a> dislocations with a Burgers vector b = a/3[$\bar{2}$113].

[29]. Thus, basal <a> dislocations and a small number of non-basal <a> dislocations seem to form during deformation of the area observed.

Fig. 9 shows TEM BF images taken under two-beam conditions of g = {0002} of three different regions. All observed dislocations must have a <c> component under this diffraction condition and they are identified as <c + a> dislocations. All the dislocations seem to be associated with the thin LPSO plates inside the α-Mg matrix. Therefore, regions which deform predominantly via basal <a> dislocations together with non-basal <a> dislocations and regions which deform predominantly by <c + a> dislocations are identified as the main deformation carriers in the α-Mg matrix that does not contain kinked LPSO plates.

4. Discussion

4.1. Deformation mechanisms of the interdendritic LPSO phase

As is evident from Fig. 3, the formation of kink bands occurs heterogeneously throughout the material during cold rolling. This may be due to the orientation dependence

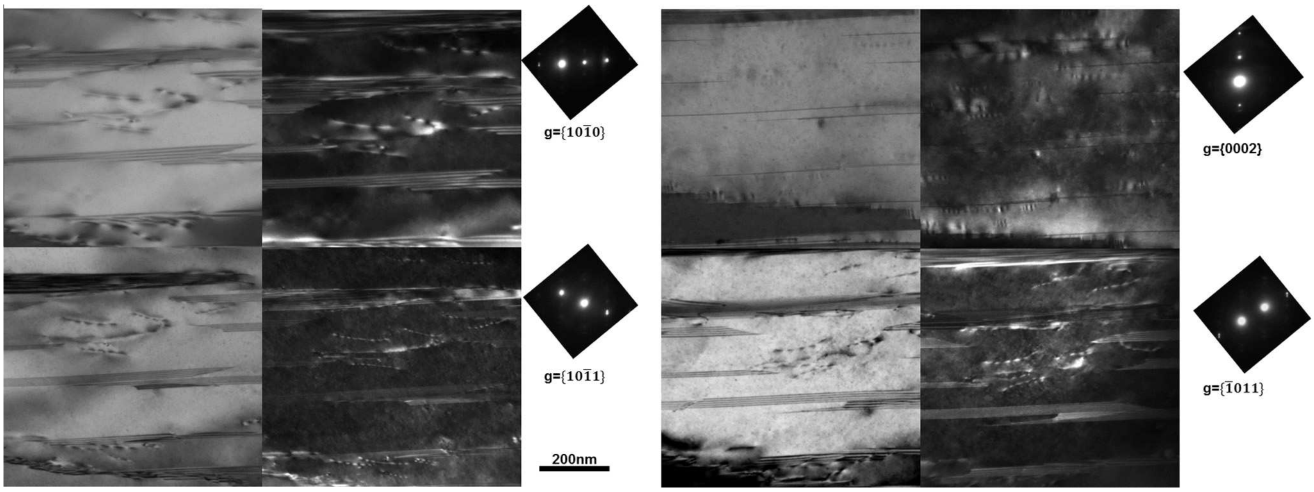

Fig. 7. TEM BF and WBDF images of 5% cold-rolled $Mg_{97}Y_2Zn_1$ alloy showing α-Mg matrix without kinked LPSO precipitates under four different two-beam conditions. The dislocations and LPSO precipitates are in contrast; under these diffraction conditions LPSO precipitates show stacking fault-like fringes.

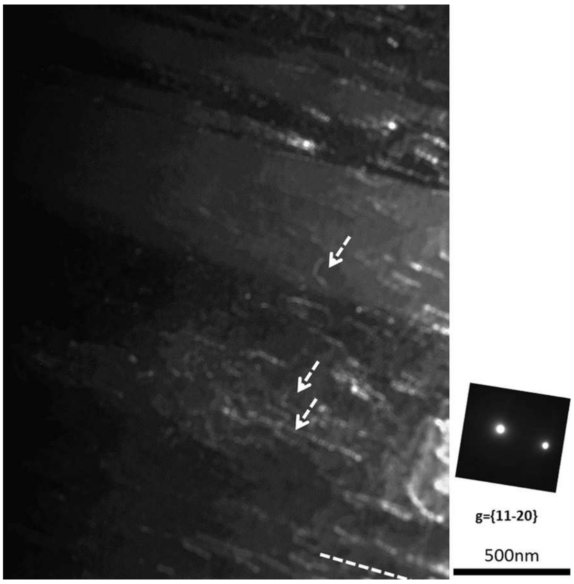

Fig. 8. TEM WBDF image of 5% cold-rolled $Mg_{97}Y_2Zn_1$ showing another region of α-Mg matrix without kinked LPSO precipitates. The basal plane trace is indicated by a white dashed line while some dislocation segments out of the basal plane are indicated by white arrows.

of the ease of basal slip. Hagihara et al. [18] reported that basal slip occurred mainly in grains with an "easy" orientation for basal slip, while deformation kinks were generated when the Schmid factor for basal slip was low. However, in the present study, such texture effects on the observed deformation characteristics were not observed since all investigated grains were similarly oriented. In order to gain deeper insight into the relationship between grain orientations and the formation of kink bands, more quantitative EBSD studies are planned for the Mg-LPSO alloys. Since the formation of kink bands can be regarded as lattice reorientation to facilitate basal slip in continued loading [30], basal <a> dislocations are observed inside the kinked LPSO phase as shown in Fig. 4b. The formation of kink bands contributes kinematically to the accommodation of a <c> axis deformation component complying with the compressive deformation state imposed in this study. As seen in Fig. 3c and d, the width and angle of the kink bands differ from region to region. According to Frank and Stroh [31], a kink boundary forms by the collapse of a number of walls into a thin region. Therefore, a high kinking angle may imply a high degree of collapse or coalescence of walls by high localized stresses. In addition, the kinking width is known to be inversely proportional to the shear yield stress of the material [32]. For example, the region shown in Fig. 3c is expected to be subjected to a large local shear

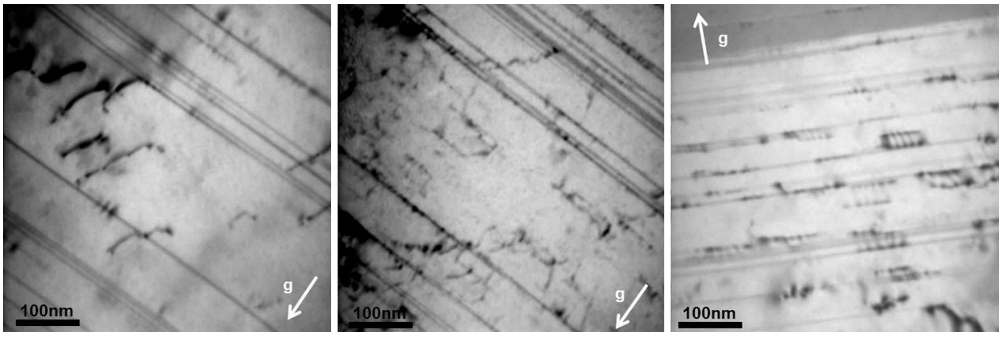

Fig. 9. TEM BF images in two-beam conditions of $g = \{0002\}$ at three different regions of 5% cold-rolled $Mg_{97}Y_2Zn_1$. <c + a> dislocations are in contrast near the thin LPSO plates.

stress due to its smaller kinking width and higher kinking angle when compared to the region observed in Fig. 3d.

Fig. 5a shows the formation of a dislocation wall by the activation of basal <a> slip inside the LPSO phase without kink bands. Two kinds of interpretation are conceivable. Firstly, the formation of the observed dislocation wall may be an independent deformation mechanism which is not connected with the formation of kink bands. Due to the crystal structure, basal <a> slip is the easiest slip system in the LPSO phase, and a dislocation wall can be formed by <a> dislocations from different parallel basal glide planes. The dislocation wall is a low-energy dislocation configuration; hence, dislocations might form a low-angle grain boundary to reduce the elastic distortion. Dislocation interaction is very unlikely since only basal slip on parallel slip planes is active. Secondly, the dislocation wall might be a precursor for the formation of kink bands since a kink boundary is composed of basal <a> dislocations [22,33]. It should be noted here that the two views do not mutually exclude each other. As reported above, the observed dislocation wall carries a crystallographic misorientation across it, and hence even at this stage acts as a geometrical discontinuity. Barsoum et al. [30] introduced the concept of incipient kink bands (IKBs). This term denotes a kink band for which the dislocation walls remain attached at its ends. At high stresses, the walls bounding the IKBs can detach, and coalescence of walls can result in the formation of kink bands.

It should be also noted, as seen in Figs. 4 and 5, that the Y- and Zn-depleted α-Mg layers preserve their characteristics during the deformation. We hence suggest that the softer Mg layers might act as mechanical buffer zones, impeding crack penetration among harder LPSO structures as observed in the case of maraging TRIP steel [34].

4.2. Deformation mechanisms of α-Mg matrix

4.2.1. Non-basal dislocations

The active deformation mechanisms in the α-Mg matrix are characterized by regions with dominant activation of basal <a> dislocations and non-basal <a> dislocations, and regions with dominantly <c + a> dislocations. Most wrought Mg alloys deform by basal slip and deformation twinning since the basal slip is the easiest slip system due to its low CRSS [35]. However, basal shear provides only two independent slip systems, far fewer than the five independent slip systems that are necessary for arbitrary homogeneous deformation in the von Mises sense [36]. In hexagonal close-packed (hcp) metals, strain along the c-axis can be accommodated only by twinning and <c + a> slip [37]. In the case of Mg-LPSO alloy, the role of <c + a> dislocations can be more significant in order to accommodate c-axis deformation since the LPSO phase is reported to hinder the formation of deformation twinning [18] due to the change in the atomic arrangement and segregation of Y and Zn atoms to specific layers. This is consistent with the present study, where no deformation twinning was observed.

Some possible explanations are suggested for the activation of <c + a> dislocations in this alloy. One possible reason is the solid solution of Y atoms in the α-Mg matrix. Sandlöbes et al. [38,39] reported that the enhanced ductility of Mg–Y alloy was caused by a high activity of pyramidal <c + a> dislocations. Another possible reason is the existence of thin LPSO plates in the α-Mg matrix. Matsuda et al. [20] investigated the dislocation structures in rapidly solidified $Mg_{97}Y_2Zn_1$ ribbons containing the LPSO phase. They reported that a number of <c + a> dislocations were visible without basal <a> dislocations in grains with LPSO precipitates, whereas only basal <a> dislocations were found in grains without LPSO precipitates. They suggested that the CRSS of the basal slip increased by the formation of LPSO precipitates. However, it is not clear why and how the existence of the LPSO phase could increase the CRSS of basal dislocation slip. Another possible explanation for the activation of <c + a> dislocations associated with thin LPSO plates is suggested as follows. During the deformation of the α-Mg matrix with thin platelet-shaped LPSO precipitates, deformation along the <a> axis can be easily accommodated since basal slip can occur easily in both phases due to the orientation relationship between α-Mg and LPSO precipitates as shown in the present study. However, deformation along the <c> axis cannot be accommodated easily due to the high CRSS for the activation of pyramidal <c + a> dislocations. It should be noted that the deformation of the α-Mg matrix with thin LPSO plates can be viewed as a co-deformation scenario of a two-phase material with the hard LPSO plates being embedded inside the soft α-Mg matrix. Ashby et al. [40] mentioned that free surfaces, grain boundaries and interface boundaries are potential sources for dislocations. They also mentioned that the highest stresses in a plastic crystal containing hard particles generally occur at the interfaces between particle and matrix, due to the discontinuity of the elastic properties there [41]. Therefore, it is possible that dislocations are generated due to elastic modulus mismatch. Recently, Tane et al. [42] reported that the Young's modulus and shear modulus of LPSO structures are clearly higher than those of pure Mg in all loading directions. The existence of interface boundaries can, hence, lead to a strong partitioning of stress to the hard LPSO phase, and of strain to the less stiff α-Mg matrix. Therefore, in order to accommodate large strains along the c-axis partitioned to the α-Mg matrix, we assume that <c + a> dislocations can be generated at the interfaces between α-Mg and LPSO phase. This suggests that the thin LPSO precipitates in the α-Mg matrix may play an important role for the improvement of ductility of the material by enhancing the activity of non-basal dislocation slip.

4.2.2. Basal I_2 stacking fault energy (SFE) of α-Mg matrix

There have been many attempts to estimate the basal I_2 SFE of Mg-LPSO alloys due to its importance for the deformation mechanisms. Zhu et al. [17] reported that the basal I_2 SFE of a solution-treated Mg–8Y–2Zn–0.6Zr (wt.%) alloy was in the range of 0.9–1.8 mJ m^{-2} based on the equilibrium separation distance of the two Shockley partial dislocations. Zhang et al. [43] suggested that the basal I_2 SFE in Mg–Y–Zn solid-solution alloys was decreased by the simultaneous addition of Y and Zn according to their predictions by density functional theory calculations. Recently, Yang et al. [24] estimated the basal I_2 SFE to be in the range of 4.0–10.3 mJ m^{-2} after deformation of $Mg_{97}Zn_1Y_2$ at 300 °C.

In the present TEM study, no dislocation dissociation and basal I_2 stacking faults are found. Fig. 10 shows a comparison of TEM WBDF images of the present $Mg_{97}Y_2Zn_1$ alloy and a Mg–3 wt.% Y solid-solution alloy. In the

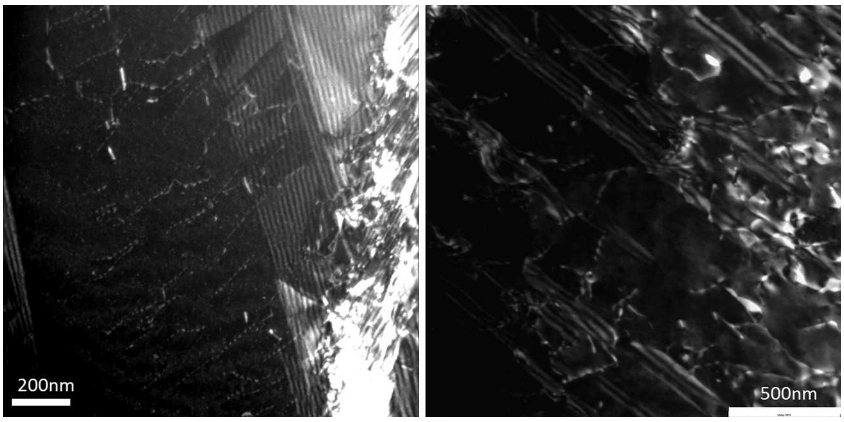

Fig. 10. TEM WBDF images of (a) 5% cold-rolled $Mg_{97}Y_2Zn_1$ alloy showing α-Mg matrix with a high density of perfect basal <a> dislocations, and (b) 3% cold-rolled Mg–3 wt.% Y solid-solution alloy showing α-Mg matrix with a high density of basal stacking faults.

left-hand side TEM micrograph of the Mg–Y–Zn alloy, a fairly high dislocation density of perfect basal <a> dislocations is observed close to the LPSO plates, which show oscillation contrast under the selected diffraction conditions. On the other hand, the right-hand side TEM image of the Mg–Y alloy shows the activation of a high density of basal I_2 stacking faults due to the decreased basal I_2 SFE caused by the addition of Y atoms [17,38,39,43]. The fact that we observe no clear partial dislocations and basal stacking faults in the Mg–Y–Zn alloy suggests that the basal I_2 SFE of the α-Mg matrix might be higher than the value estimated from previous research. The high density of thin LPSO precipitates inside the α-Mg matrix might result in locally different values of the basal I_2 SFE in the matrix and the thin LPSO precipitates. This affects both the elemental partitioning and, hence, the true local composition and the micromechanical elastic stress states in the material. From the SEM-EDS result, the average chemical composition of the α-Mg is determined to be Mg–0.56Y–0.26Zn (at.%). However, those Y and Zn atoms which exist inside the α-Mg matrix are in part partitioned to the thin LPSO plates (Fig. 2c). Thus, the actual composition and consequently the basal I_2 SFE of the Y- and Zn-depleted α-Mg matrix is probably more similar to that of pure Mg.

From the present study, the Mg matrix can be interpreted as a two-phase material containing thin (~3–5 nm) platelet-shaped LPSO precipitates and α-Mg matrix grains. The preferential partitioning of Y and Zn atoms into the thin LPSO plates results in a reduction in their basal I_2 SFE, while the α-Mg matrix, with its depletion in Y and Zn, has a higher basal I_2 SFE than the thin LPSO plates. This analysis is consistent with the suggestion of Zhu et al. [15] that the phase transformation from basal stacking faults to LPSO structures can occur by the formation of overlapping stacking faults having the correct spacing and subsequent diffusion-controlled segregation to the faults. This finding suggests that the basal I_2 SFE of the α-Mg matrix strongly depends on the local chemical composition and can be modified, and hence designed, via material processing.

5. Conclusions

We have examined the room temperature deformation mechanisms of a cold-rolled $Mg_{97}Y_2Zn_1$ alloy with respect to both the α-Mg matrix and the interdendritic LPSO phase using TEM. The following conclusions are drawn:

1. The solution-treated material consists of an interdendritic 18R phase and α-Mg matrix with a high density of thin (~3–5 nm) platelet-shaped LPSO precipitates.
2. Two different preferential deformation modes are observed in the interdendritic LPSO phase: (i) kink bands in conjunction with basal <a> dislocations; and (ii) basal <a> slip and the formation of dislocation walls.
3. The dominant deformation modes of the α-Mg matrix LPSO precipitates are observed to be twofold: (i) regions which deform predominantly by basal <a> slip and non-basal <a> slip; and (ii) regions which deform predominantly by pyramidal <c + a> slip. The elastic modulus mismatch between α-Mg matrix and LPSO plates is suggested to be the main source of activating non-basal dislocations. No twinning was found up to 5% engineering strain.
4. The α-Mg matrix without basal stacking faults shows no evidence of a lowered basal I_2 SFE. Partitioning of Y and Zn atoms from the α-Mg matrix into the LPSO precipitates can lead to locally different chemical compositions and, consequently, different values of the basal I_2 SFE.

Acknowledgements

The authors are grateful for the kind support of the Alexander von Humboldt Stiftung (AvH, Alexander von Humboldt Foundation, www.humboldtfoundation.de) for J.K.K.

References

[1] B.L. Mordike, T. Ebert, Mater. Sci. Eng. A 302 (2001) 37.
[2] Y. Kawamura, K. Hayashi, A. Inoue, T. Masumoto, Mater. Trans. 42 (2001) 1172.
[3] Y. Kawamura, M. Yamasaki, Mater. Trans. 48 (2007) 2986.
[4] M. Noda, T. Mayama, Y. Kawamura, Mater. Trans. 50 (2009) 2526.
[5] B. Chen, D. Lin, X. Zeng, C. Lu, J. Mater. Sci. 45 (2010) 2510.
[6] M. Yamasaki, K. Hashimoto, K. Hagihara, Y. Kawamura, Acta. Mater. 59 (2011) 3646.
[7] T. Itoi, T. Inazawa, M. Yamasaki, Y. Kawamura, M. Hirohashi, Mater. Sci. Eng. A 560 (2013) 216.
[8] E. Abe, A. Ono, T. Itoi, M. Yamasaki, Y. Kawamura, Philos. Mag. Lett. 91 (2011) 690.

[9] D. Egusa, E. Abe, Acta. Mater. 60 (2012) 166.
[10] T. Itoi, T. Seimiya, Y. Kawamura, M. Hirohashi, Scripta. Mater. 51 (2004) 107.
[11] X. Shao, H. Yang, J.T. De Hosson, X. Ma, Microsc. Microanal. 19 (2013) 1575.
[12] Y.M. Zhu, A.J. Morton, J.F. Nie, Acta. Mater. 58 (2010) 2936.
[13] Y.M. Zhu, M. Weyland, A.J. Morton, K. Oh-ishi, K. Hono, J.F. Nie, Scripta. Mater. 60 (2009) 980.
[14] M. Matsuda, S. Ii, Y. Kawamura, Y. Ikuhara, M. Nishida, Mater. Sci. Eng. A 393 (2005) 269.
[15] Y.M. Zhu, A.J. Morton, J.F. Nie, Acta. Mater. 60 (2012) 6562.
[16] K. Hagihara, A. Kinoshita, Y. Sugino, M. Yamasaki, Y. Kawamura, H.Y. Yasuda, et al., Acta. Mater. 58 (2010) 6282.
[17] Y.M. Zhu, A.J. Morton, M. Weyland, J.F. Nie, Acta. Mater. 58 (2010) 464.
[18] K. Hagihara, N. Yokotani, Y. Umakoshi, Intermetallics 18 (2010) 267.
[19] K. Hiraga, A. Yasuhara, K. Saito, Mater. Trans. 53 (2012) 1385.
[20] M. Matsuda, S. Ando, M. Nishida, Mater. Trans. 46 (2005) 361.
[21] E. Oñorbe, G. Garcés, P. Pérez, P. Adeva, J. Mater. Sci. 47 (2011) 1085.
[22] X.H. Shao, Z.Q. Yang, X.L. Ma, Acta. Mater. 58 (2010) 4760.
[23] M. Yamasaki, K. Hagihara, S-i. Inoue, S-i. Inoue, J.P. Hadorn, Y. Kawamura, Acta. Mater. 61 (2013) 2065.
[24] Z. Yang, M.F. Chisholm, G. Duscher, X. Ma, S.J. Pennycook, Acta. Mater. 61 (2013) 350.
[25] E. Abe, Y. Kawamura, K. Hayashi, A. Inoue, Acta. Mater. 50 (2002) 3845.
[26] Y. Chino, M. Mabuchi, S. Hagiwara, H. Iwasaki, A. Yamamoto, H. Tsubakino, Scr. Mater. 51 (2004) 711.
[27] M. Matsuda, S. Ii, Y. Kawamura, Y. Ikuhara, M. Nishida, Mater. Sci. Eng. A 386 (2004) 447.
[28] D. Egusa, M. Yamasaki, Y. Kawamura, E. Abe, Mater. Trans. 54 (2013) 698.
[29] J.P. Hadorn, R.P. Mulay, K. Hantzsche, S. Yi, J. Bohlen, D. Letzig, et al., Metall. Mater. Trans. A 44 (2013) 1566.
[30] M.W. Barsoum, T. Zhen, S.R. Kalidindi, M. Radovic, A. Murugaiah, Nat. Mater. 2 (2003) 107.
[31] F.C. Frank, A.N. Stroh, Proc. Phys. Soc. B 65 (1952) 811.
[32] B. Budianski, N.A. Fleck, Appl. Mech. Rev. 47 (1993) S246.
[33] M.W. Barsoum, L. Farber, T. El-raghy, Metall. Mater. Trans. A 30 (1999) 1727.
[34] D. Raabe, S. Sandlöbes, J. Millán, D. Ponge, H. Assadi, M. Herbig, P.P. Choi, Acta. Mater. 61 (2013) 6132.
[35] H.E. Friedrich, B.L. Mordike, Magnesium Technology: Metallurgy, Design Data, Automotive Applications, Springer Verlag, Berlin, 2006.
[36] J. Koike, T. Kobayashi, T. Mukai, H. Watanabe, M. Suzuki, K. Maruyama, et al., Acta. Mater. 51 (2003) 2055.
[37] M.H. Yoo, Metall. Trans. A 12 (1981) 409.
[38] S. Sandlöbes, M. Friák, S. Zaefferer, A. Dick, S. Yi, D. Letzig, et al., Acta. Mater. 60 (2012) 3011.
[39] S. Sandlöbes, S. Zaefferer, I. Schestakow, S. Yi, R. Gonzalez-Martinez, Acta. Mater. 59 (2011) 429.
[40] M.F. Ashby, S.H. Gelles, L.E. Tanner, Philos. Mag. 19 (1969) 757.
[41] M.F. Ashby, Philos. Mag. 21 (1970) 399.
[42] M. Tane, Y. Nagai, H. Kimizuka, K. Hagihara, Y. Kawamura, Acta. Mater. 61 (2013) 6338.
[43] Q. Zhang, L. Fu, T.-W. Fan, B.-Y. Tang, L.-M. Peng, W.-J. Ding, et al., Phys. B Condens. Matter 416 (2013) 39.